Efficient wide-bandgap perovskite photovoltaics with homogeneous halogen-phase distribution

Rui Wang[1,10], Xiaoyu Liu[1,10], Shan Yan[1,10], Ni Meng[1], Xinmin Zhao[1], Yu Chen[2], Hongxiang Li[3], Saif M. H. Qaid[4], Shaopeng Yang[1] ✉, Mingjian Yuan[5] & Tingwei He[1,6,7,8,9] ✉

Wide-bandgap (WBG) perovskite solar cells (PSCs) are employed as top cells of tandem cells to break through the theoretical limits of single-junction photovoltaic devices. However, WBG PSCs exhibit severe open-circuit voltage (V_{oc}) loss with increasing bromine content. Herein, inhomogeneous halogen-phase distribution is pointed out to be the reason, which hinders efficient extraction of carriers. We thus propose to form homogeneous halogen-phase distribution to address the issue. With the help of density functional theory, we construct a double-layer structure (D-2P) based on 2-(9H-Carbazol-9-yl)ethyl] phosphonic acid molecules to provide nucleation sites for perovskite crystallization. Homogeneous perovskite phase is achieved through bottom-up templated crystallization of halogen component. The efficient carrier extraction reduces the Shockley-Read-Hall recombination, resulting in a high V_{oc} of 1.32 V. As a result, D-2P-treated device (1.75 eV) achieves a record power conversion efficiency of 20.80% (certified 20.70%), which is the highest value reported for WBG (more than 1.74 eV) PSCs.

Mixed-halogen wide-bandgap (WBG) perovskite materials is often employed as the top cells of tandem solar cells, by combining with narrow-bandgap (NBG) bottom cells such as silicon solar cells, organic solar cells, tin-lead hybrid perovskites solar cells (PSCs), etc[1–6]. Due to the strong photon absorption capability in the long-wavelength range, the bottom cells are beneficial to obtain a larger photocurrent, but usually exhibit a low photovoltage. It is crucial for tandem cells to achieve the largest possible voltage output through WBG top cells[7]. Nevertheless, WBG PSCs suffer from severe open-circuit voltage (V_{oc}) loss compared to NBG photovoltaic devices[8]. Minimizing the V_{oc} loss

of WBG PSCs should be one of the important issues that need to be addressed urgently in the field of efficient tandem solar cells[9,10].

Inorganic nickel oxide (NiO_x) film is often employed as hole transport layers (HTL) in WBG PSCs due to its remarkable thermal stability, chemical stability, and high light transmittance[11,12]. It is well known that high defect states and mismatched energy levels alignment at the interface between NiO_x HTL and perovskite, results in a low V_{oc}[13]. The application of self-assembled monolayer (SAM) is an important attempt to solve this problem, which has greatly improved the V_{oc} of the PSCs[14–16]. Despite this, there is still a large V_{oc} loss in WBG PSCs,

[1]College of Physics Science and Technology, Hebei University, Baoding 071002, China. [2]Beijing Synchrotron Radiation Facility, Institute of High Energy Physics, CAS, Beijing 100049, China. [3]College of Polymer Science and Engineering State Key Laboratory of Polymer Materials Engineering, Sichuan University, Chengdu 610065, China. [4]Department of Physics & Astronomy, College of Sciences, King Saud University, Riyadh, Saudi Arabia. [5]College of Chemistry, Nankai University, Tianjin 300071, China. [6]Hebei Key Laboratory of Optic-Electronic Information and Materials, Hebei University, Baoding 071002, China. [7]National-Local Joint Engineering Laboratory of New Energy Photoelectric Devices, Hebei University, Baoding 071002, China. [8]Province-Ministry Co-construction Collaborative Innovation Center of Hebei Photovoltaic Technology, Hebei University, Baoding 071002, China. [9]Institute of Life Science and Green Development, Hebei University, Baoding 071002, China. [10]These authors contributed equally: Rui Wang, Xiaoyu Liu, Shan Yan. ✉e-mail: spyang@hbu.edu.cn; htw2022@hbu.edu.cn

according to the Shockley-Queisser (S-Q) limit efficiency theory[17]. As the optical bandgap of perovskite material widens, the bromine (Br) content of films inevitably increases, and the resulting device exhibits increasingly severe V_{oc} loss[18].

It is generally recognized that phase separation of perovskite films during the crystallization process is a prominent problem leading to large V_{oc} loss, especially in perovskite systems with Br content exceeding 20 mol%[7,19]. Br-based perovskites possess lower solubility than iodine (I)-based analogues, making it easier to nucleate and grow rapidly[7]. Therefore, for the commonly used solution method, the Br-rich perovskite phase preferentially crystallizes at the perovskite/air interface at the top of the film, while the I-rich phase is deposited at the bottom of the film[20]. Such asynchronous crystallization is the root cause of perovskite phase separation. Inhomogeneous phase distribution impairs efficient extraction and collection of carriers, leading to the severe nonradiative recombination, which has been demonstrated in quasi-two-dimensional perovskite systems and formamidine (FA) perovskite systems[21–24]. Thus, regulating the crystallization kinetics of mixed-halogen perovskites, and achieving homogeneous halogen-phase distribution should be an important strategy to reduce the V_{oc} loss of WBG PSCs.

Based on the above inspiration, it is an ideal choice to prepare a functionalized molecular layer that acts on the buried interface of perovskite film to regulate the crystallization behavior of halides. Considering the advantages of SAM molecules in passivating defects of NiOx film, we envision to construct a double-layer SAM film at the interface between HTL and perovskite. With the help of density functional theory (DFT) calculations, we have successfully achieved a double-layer structure (D-2P) based on a single-layer 2-(9H-Carbazol-9-yl)ethyl]phosphonic acid (S-2P) molecules. D-2P structure could be formed through the strong π-π interaction between the carbazole groups located at the head end of the S-2P molecule[16,25,26]. Meanwhile, the phosphate group located at the tail end of the S-2P molecule can anchor the NiOx and the $[PbX_6]^{4-}$ octahedron respectively, thereby forming a stable bond bridge structure[27,28]. More importantly, the phosphate group acts on the $[PbX_6]^{4-}$ octahedron through -P-OH···X bonds, reducing the formation energy of Br-phase and I-phase perovskite simultaneously. The nucleation sites provided by the D-2P structure induce bottom-up homogeneous crystallization of the halogen component. The reversed crystallization process and homogeneous halogen-phase distribution have been demonstrated through in-situ grazing-incident wide-angle X-ray scattering (GIWAXS) and depth-profiling X-ray photoelectron spectroscopy (XPS) characterization, etc. Benefiting from optimized energy level alignment and efficient carrier extraction, non-radiative recombination is effectively suppressed. As a result, D-2P-treated WBG PSCs (1.75 eV) achieved a record power conversion efficiency (PCE) of 20.80% (certified 20.70%), accompanied by a high V_{oc} of 1.32 V. And a semitransparent PSC was employed as four-terminal (4 T) perovskite/perovskite tandem with a PCE of 28.08%. Furthermore, the homogeneous phase distribution alleviated the lattice strain of the WBG perovskite film and ensured the long-term operational stability. The unencapsulated device still maintains more than 90% of the original PCE after being stored under nitrogen conditions for 2500 h.

Results

Halogen-phase separation issue and D-2P structure construction

Previous reports have demonstrated that homogeneous phase distribution in perovskite films is crucial to achieve high-performance photovoltaic devices[19]. Therefore, we investigate the phase distribution of mixed-halide WBG perovskite films based on a common $FA_{0.8}Cs_{0.15}MA_{0.05}Pb(I_{0.7}Br_{0.3})_3$ system (1.75 eV). In-situ GIWAXS technique is an effective characterization to reveal the crystallization dynamics of perovskite films. Various grazing incidence angles (θ) are applied to detect crystal structure information at different depths of

perovskite films[29]. As shown in Fig. 1a, the (001) plane of the S-2P-treated perovskite film corresponds to a constant q value at 1.03 nm⁻¹ when the top of the film ($\theta = 0.3°$) was probed during the spin-coating stage. Crystallization situation at the bottom of the film can also be detected by increasing the grazing incidence angle ($\theta = 1°$), and a broader diffraction signal was showed in Fig. 1b. Moreover, the q value continuously decreases from 1.03 to 1.01 nm⁻¹ throughout the spin-coating stage. Considering that perovskite films preferentially crystallize at the air/solution interface[20], the initial GIWAXS signal should mainly depend on the crystal structure of the film surface (Fig. 1d). As the film crystallizes sequentially from top to bottom, the crystal structure at the bottom begins to dominate the GIWAXS signal. The decreased q value represents that the perovskite at the bottom film possesses a larger interplanar spacing than at the top film. The q values at the top and bottom films are almost constant during the annealing stage (Supplementary Fig. 1), indicating that an inhomogeneous perovskite phase is formed during the spin-coating stage.

We further qualitatively analyzed the phase distribution of perovskite films by depth-profiling XPS spectra (Fig. 1c). As the profiling depth increases, the intensity of I $3d_{5/2}$ and I $3d_{3/2}$ spectra (619.5 and 631.0 eV) gradually increases, while the intensity of Br $3d_{5/2}$ and Br $3d_{3/2}$ spectra (68.6 and 69.7 eV) at the corresponding film depth gradually decreases, which is consistent with the GIWAXS results. It is easy to understand that the $[PbBr_6]^{4-}$ octahedron preferentially crystallizes on the top film, due to its solubility is lower than $[PbI_6]^{4-}$ octahedron[7]. This results in excessive consumption of the Br component, and hence the I-rich phase is deposited at the bottom film (Fig. 1d). Such phase distribution signifies an inhomogeneous energy landscape, which would lead to large V_{oc} loss and low PCE[18]. Achieving homogeneous halogen-phase distribution through crystallization kinetics regulation should be an effective strategy to address this issue.

Thereupon, we propose to construct D-2P structure based on 2P molecules to regulate the crystallization kinetics of perovskite films. D-2P structure could be formed through the strong π-π interaction between the carbazole groups located at the head end of the S-2P molecule (Fig. 1e). We used DFT calculations to simulate the binding energy of 2P pairs in three stacking model: parallel stacking, intersecting stacking, and antiparallel stackings (Fig. 1h)[30]. For parallel stacking (inset i), the benzene rings at the heads of the two 2P molecules are arranged in parallel, and the phosphate groups at their tails extend in same directions. For intersecting stacking (inset ii), the benzene rings at the heads of the two 2P molecules intersect with each other at a certain angle, and the phosphate groups at their tails extend in opposite directions. For parallel stacking (inset iii), the benzene rings at the heads of the two 2P molecules are arranged in parallel, and the phosphate groups at their tails extend in opposite directions. As shown, intersecting stacking mode exhibits a larger binding energy (10.847 eV) than parallel stacking (0.014 eV) and antiparallel stacking mode (0.018 eV), which indicates that this stacking mode should be the most stable form of D-SP structure. The electrostatic potential distribution of 2P molecules also proves that intersecting stacking is the optimal arrangement of 2P pairs (Supplementary Fig. 2).

We then construct the D-2P structure based on the ITO/ NiOx substrate by a simple solution method (Supplementary Figs. 3, 4). A thin 2P film is deposited on the NiOx layer using spin-coating method at step I (Fig. 1f). The resulting film spontaneously forms an S-2P structure, and the phosphate group located at the tail end of the oriented 2P molecule can anchor the NiOx layer[31]. Meanwhile, some non-oriented 2P molecules are inevitably attached to the surface of the S-2P structure. S-2P structure without residual molecules can be obtained by removing attached 2P molecules with the help of absolute ethanol rinse (step II). The benzene ring groups exposed on the surface of the S-2P layer increase the hydrophobicity of the film, and thus the film obtained at stage II exhibits a larger contact angle (61.9°) compared with the film (35.1°) obtained at stage I. D-2P structure can be
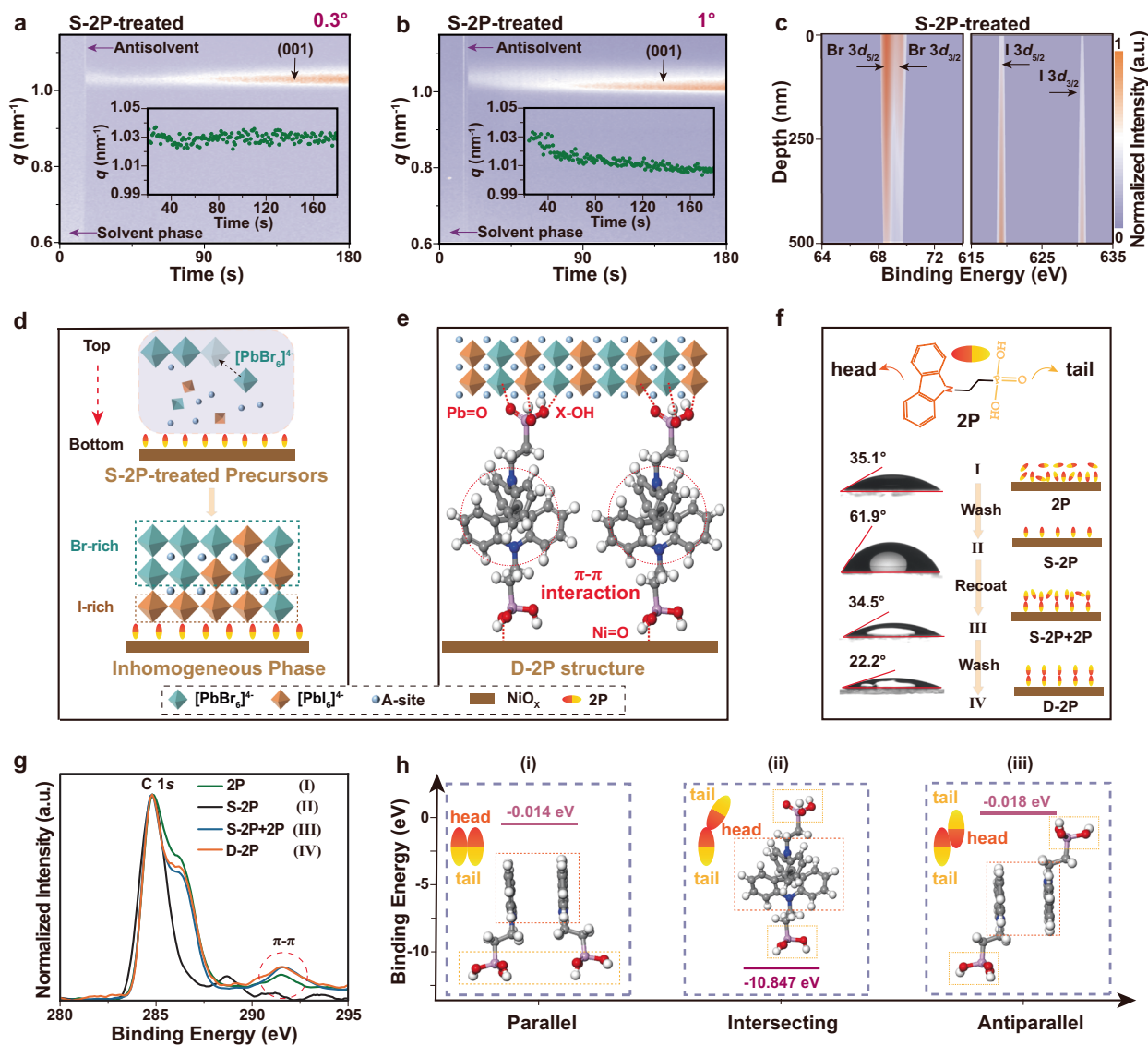
Fig. 1 | D-2P structure construction in mixed-halogen WBG perovskite system.
a, b In-situ GIWAXS patterns of S-2P-treated perovskite film with grazing incident angle of 0.3° and 1°during the spin-coating stage. Inset: the extracted q value. **c** Depth-profiling Br $3d$ and I $3d$ XPS spectra of S-2P-treated perovskite film. **d** Schematic diagram of crystallization kinetics of S-2P-treated perovskite film. **e** Schematic diagram of D-2P structure between NiO$_x$ and perovskite. **f** Construction of D-2P structure and corresponding water contact angle measurements. **g** C 1 s XPS spectra of the D-2P structure at different stages. **h** The binding energy of the D-2P structure calculated in three stacking model: (inset i) parallel stacking, (inset ii) intersecting stacking, and (inset iii) antiparallel stackings by DFT simulation.

obtained by re-depositing an anhydrous ethanol solution of 2P molecules (phase III) and rinse again (phase IV). The smallest contact angles (22.2°) can be obtained in the final film, because the intersecting π-π stacking of 2P pairs exposes the hydrophilic phosphate groups on the film surface. This strong π-π force can also be demonstrated through C 1 s spectra of XPS[16]. As shown in Fig. 1g, a peak at binding energy of 291.6 eV could be observed, which is consistent with the π-π bonding collaboration. The resulting D-2P structure (stage IV) exhibited the strongest π-π interaction. The anchoring action of Ni=O bonds between the phosphate group of the D-2P structure and the NiO$_x$ film has been demonstrated by XPS spectra (Supplementary Fig. 5), thereby forming a stable bond bridge structure.

Homogeneous halogen-phase perovskite film induced by the D-2P structure
The phosphate groups on the top layer of the D-2P structure are exposed, which is an opportunity to anchor the [PbX$_6$]$^{4-}$ octahedron (Supplementary Fig. 6) and provide nucleation sites for the crystallization of perovskite films. We then performed in-situ GIWAXS with different θ angles. The characteristic signal of ITO can be observed in the GIWAXS patterns of perovskite films ($\theta = 1°$) (Fig. 2c, Supplementary Figs. 7 and 8), indicating that the signal at the bottom of perovskite film can be detected. As shown in Fig. 2a, b, the (001) plane of the D-2P-treated perovskite film exhibited an almost constant q value of 1.02 nm^{-1} at spin-coating stage, both on the top ($\theta = 0.3°$) at and bottom ($\theta = 1°$) of the film[29,32]. The annealed perovskite film also showed an almost the same diffraction ring of (001) plane for different incident angles (Fig. 2c, Supplementary Fig. 9), meaning that the perovskite phase is uniformly distributed throughout the film. This is in sharp contrast to the inhomogeneous phase distribution exhibited by the surface and bottom of the S-2P-treated film.

Meanwhile, the strong perovskite signal at the top of the S-2P-treated perovskite film is detected earlier than that at the bottom (Fig. 2a), indicating that the perovskite crystallizes preferentially at the top. This up-bottom crystallization approach allows stronger (001) signals to be detected at the top. In general, Br-based perovskite
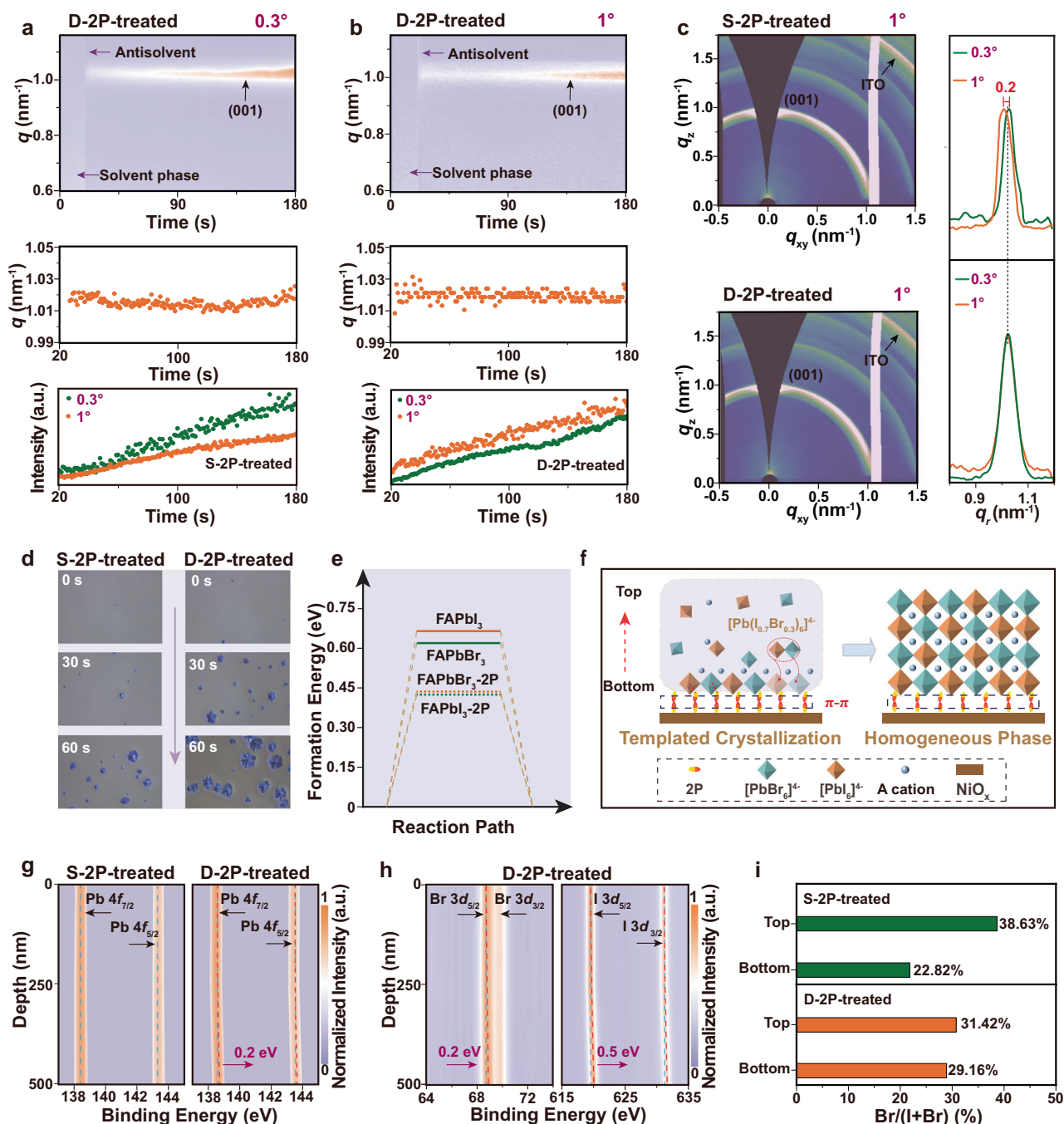
Fig. 2 | Homogeneous halogen-phase perovskite film. In-situ GIWAXS patterns and the extracted q value of D-2P-treated perovskite film with grazing incident angle of (**a**) 0.3° and (**b**) 1°during the spin-coating stage. Bottom: the extracted (001) signal intensity of S-2P-treated and D-2P-treated perovskite films. **c** GIWAXS patterns of S-2P-treated and D-2P-treated perovskite films, and corresponding 2D diagrams of extracted (001) crystal faces. **d** In-situ LSCM images of S-2P-treated and D-2P-treated perovskite films. **e** Formation energy of FAPbI$_3$ and FAPbBr$_3$ with and without 2P (2-(9H-Carbazol-9-yl)ethyl]phosphonic acid). **f** Schematic diagram of crystallization kinetics of D-2P-treated perovskite films. **g**, **h** Depth-profiling XPS spectra of Pb 4f, I 3d, and Br 3d. **i** The extracted halogen content of S-2P-treated and D-2P-treated perovskite films at top and bottom by EDS scanning.

exhibits a lower formation energy than I-based one (Fig. 2e). Thus, the Br-rich phase preferentially crystallizes at the top of the S-2P-treated perovskite film, resulting in an inhomogeneous halogen-phase distribution. In stark contrast, the strong perovskite signal was first detected at the bottom of the D-2P-treated perovskite film rather than the top (Fig. 2b). The slower crystallization rate at the top of the film results in a weaker (001) signal compared to that at the bottom. This bottom-up crystallization approach is attributed to the D-2P structure, and the phosphate group provides nucleation sites for the crystallization of perovskite films. Furthermore, the D-2P-treated perovskite

film displayed a faster crystallization rate than the S-2P-treated perovskite film, which can be determined from the faster increase in GIWAXS signal intensity of the former. The in-situ laser scanning confocal microscope (LSCM) images further supports this conclusion that shorter crystallization time is observed for the D-2P-treated perovskite film compared to S-2P-treated one (Fig. 2d and Supplementary Fig. 10).

The crystallization kinetic behavior of the above films confirms our previous assumptions. The phosphate groups exposed in the D-2P structure could simultaneously anchor the [PbI$_6$]$^{4-}$ and [PbB$_6$]$^{4-}$

through -P-OH···X⁻ and -P = O···Pb²⁺ bonds[33] (Fig. 2f). As shown in the XPS spectra of the perovskite film at the bottom, Pb 4*f*, Br 3*d* and I 3*d* peaks were all shifted towards the high energy region (Fig. 2g, h), demonstrating the strong interaction between the D-2P structure and the perovskite crystal[34]. The formation energy of I-based and Br-based perovskites could be reduced and closer after the introduction of 2P (2-(9H-Carbazol-9-yl)ethyl]phosphonic acid) (Fig. 2e). This indicates that the phosphate groups will interact with both I and Br components and provide nucleation sites for perovskite crystallization, which will induce the homogeneous crystallization of the halogen phase. As expected, depth-profiling XPS spectra showed the same Br 3*d* and I 3*d* signal intensity at various depths of the film (Fig. 2h, Supplementary Fig. 11). Moreover, the double-layered materials based on other carbazole-based phosphonic acids also showed similar effects, such as such as [2-(3,6-dimethoxy-9H-carbazol-9-yl)ethyl]phosphonic acid (2M) and [4-(3,6-dimethoxy-9H-carbazol-9-yl) butyl]phosphonic acid (4M) (Supplementary Figs. 12, 13).

We further quantitatively analyzed the halogen content based on the focused ion beam (FIB)-prepared flakes located on the top and bottom of the perovskite film[35]. As shown in the energy dispersive spectroscopy (EDS) combined transmission electron microscopy (TEM) (Supplementary Fig. 14), the S-2P-treated films exhibited distinguishable Br/(I+Br) ratios for the top (38.63%) and bottom (22.82%) samples. In contrast, a close to theoretical Br/(I+Br) ratio (30%) is detected for both the top (31.42%) and bottom (29.16%) samples treated with D-2P structure (Fig. 2i). The same conclusion can be obtained through the statistical Br/(I+Br) ratio at different spatial positions (Supplementary Fig. 15). Such halogen-phase distribution is attributed to the anchoring effect of the D-2P structure on the buried interface of perovskite film.

Carrier transport behavior of homogeneous halogen-phase perovskite film

We then investigated the carrier transport behavior at the top and bottom of the perovskite film. Kelvin probe force microscopy (KPFM) provides a channel to detect the surface electronic state information of perovskite films. According to previously reported methods[36], we stripping perovskite films form substrates (Supplementary Figs. 16, 17). EDS mapping of the substrate after stripping exhibited that the signal of the Pb element is negligible (Supplementary Fig. 18), indicating that the complete perovskite film is stripped, which allows the information at the bottom of the film to be effectively detected. As shown in Fig. 3a–c, similar to the top film, the bottom film also exhibits a uniform potential distribution in different regions. This also proves that the bottom films of two perovskite samples exhibit almost negligible crystal damage after peeling off. Moreover, the top (0.482 V) exhibited significantly larger contact potential difference (CPD) than the bottom (0.188 V) of S-2P-treated perovskite film. This is exactly in line with the situation caused by halogen-phase segregation[37,38]. In contrast, the D-2P-treated perovskite film exhibited close CPD at the top (0.251 V) and bottom (0.223 V), and more uniform CPD distribution further confirmed the homogeneous halogen-phase distribution throughout the perovskite film. In general, changes in the CPD of films are accompanied by rearrangements of the energy landscape.

Thereupon, we measured the ultraviolet-visible (UV-vis) absorption spectra (Supplementary Fig. 19) and the ultraviolet photoelectron spectroscopy (UPS) of the films to characterize the energetics (Fig. 3d–f). Considering that long-term UV-light irradiation would damage the perovskite film[39], we peeled the buried bottom surface of the perovskite film off the substrate to minimize the error in UPS measurements. As displayed on the bottom of films, the D-2P-treated perovskite film possessed a shallower Fermi level (5.0 eV) than the S-2P-treated film (5.4 eV), showing more N-type characteristics[40], which is beneficial to achieving high V_{oc}. Moreover, the valence band maximum (VBM) of the former is closer to the highest occupied molecular

orbital (HOMO) of 2P molecule[10], and optimized energy level alignment is achieved between the photoactive layer and the hole transport layer. Moreover, the top of the S-2P-treated perovskite film showed more Br components than the D-2P-treated film, which means a larger E_g. The former exhibited smaller E_{VBM} value than the latter according to their UPS measurements (Supplementary Fig. 20). Therefore, we can deduce that the D-2P-treated perovskite film possessed a larger E_{CBM} value than the S-2P-treated one. This is a smaller energy barrier between the perovskite film and the electron transport layer, which is conducive to electron extraction[41].

The matched energy level structure ensures effective carrier extraction. The steady-state photoluminescence (PL) spectra of ITO/NiO$_x$/D-2P/Perovskite film showed a lower PL intensity than that of ITO/NiO$_x$/S-2P/Perovskite film (Fig. 3g). And a full width at half maxima (FWHM) could also be observed, which is closely related to the homogeneous halogen-phase. In general, low PL intensity may be caused by the following two factors. In the first case, the high defect states lead to strong PL quenching in perovskite films[42]. We then measured the defect states of two perovskite films using thermal admittance spectroscopy (TAS)[43]. As shown, Band 1 (< 0.4 eV) represents shallow level, Band 2 (0.4–0.5 eV) and Band 3 (> 0.5 eV) represent deep level (Supplementary Fig. 21). Deep level defects are the main factors affecting device performance. The density of defect states (*t*DOS) was in the order of 10^{16} to 10^{19} m⁻³ eV⁻¹ in the both devices. Meanwhile, the D-2P-treated perovskite device displayed the reduced *t*DOS over the entire trap depth compared with S-2P-treated film. Therefore, we can confirm that the low defect state of the D-2P-treated perovskite film is not responsible for the low PL intensity. For the second case, the rapid hole extraction from the perovskite film to the hole transport layer film induces strong PL quenching[44,45]. As shown in Fig. 3d–f, the valence band maximum (VBM) of the D-2P-treated perovskite film is closer to the highest occupied molecular orbital (HOMO) of 2P molecule, compared with that the S-2P-treated perovskite film. The optimized energy level alignment between the photoactive layer and the hole transport layer ensures a more efficient hole extraction rate, which can be the reason for the low PL intensity. We then operated solar cells as light-emitting diodes (Supplementary Fig. 22), and D-2P-treated PSC device showed enhanced electroluminescence (EL) intensity compared with S-2P-treated one. This directly demonstrates that non-radiative recombination at the interface between the perovskite and the transport layer is reduced in the D-2P-treated devices.

Furthermore, we measured the confocal laser microscopy (TCFM) mappings of the films to study the carrier lifetime distribution in different regions. As shown in Fig. 3h, i, the overall fluorescence lifetime of the D-2P-treated film is nearly an order of magnitude lower than that of the S-2P-treated film. The corresponding time-resolved PL (TRPL) decay also exhibited the same trend (Supplementary Fig. 23). Benefiting from the templated crystallization induced by the D-2P structure, the high-quality and homogeneous halogen-phase perovskite film exhibited the efficient carrier extraction (Supplementary Fig. 24). Therefore, the improved optical and electrical properties lay a solid foundation for the efficient photovoltaic devices.

Relationship between homogeneous halogen phase and the V_{oc} loss

We fabricated a p-i-n planar heterojunction WBG PSCs (1.75 eV) with an architecture of ITO/NiO$_x$/D-2P(S-2P)/Perovskite/PEAI/C$_{60}$/BCP/Ag. The S-2P-treated PSC showed a PCE of 18.33% with a low V_{oc} of 1.25 V (Fig. 4a). In contrast, the optimized D-2P-treated PSC achieved a champion PCE of 20.80% (Supplementary Fig. 25, Supplementary Table 1). And a certified PCE of 20.7% was obtained at SIMIT (Fig. 4b, Supplementary Fig. 26), which is the highest value reported for a WBG PSC with a bandgap wider than 1.74 eV (Fig. 4c, Supplementary Table 2). A short-circuit current density (J_{sc}) of 18.81 mA cm⁻² obtained
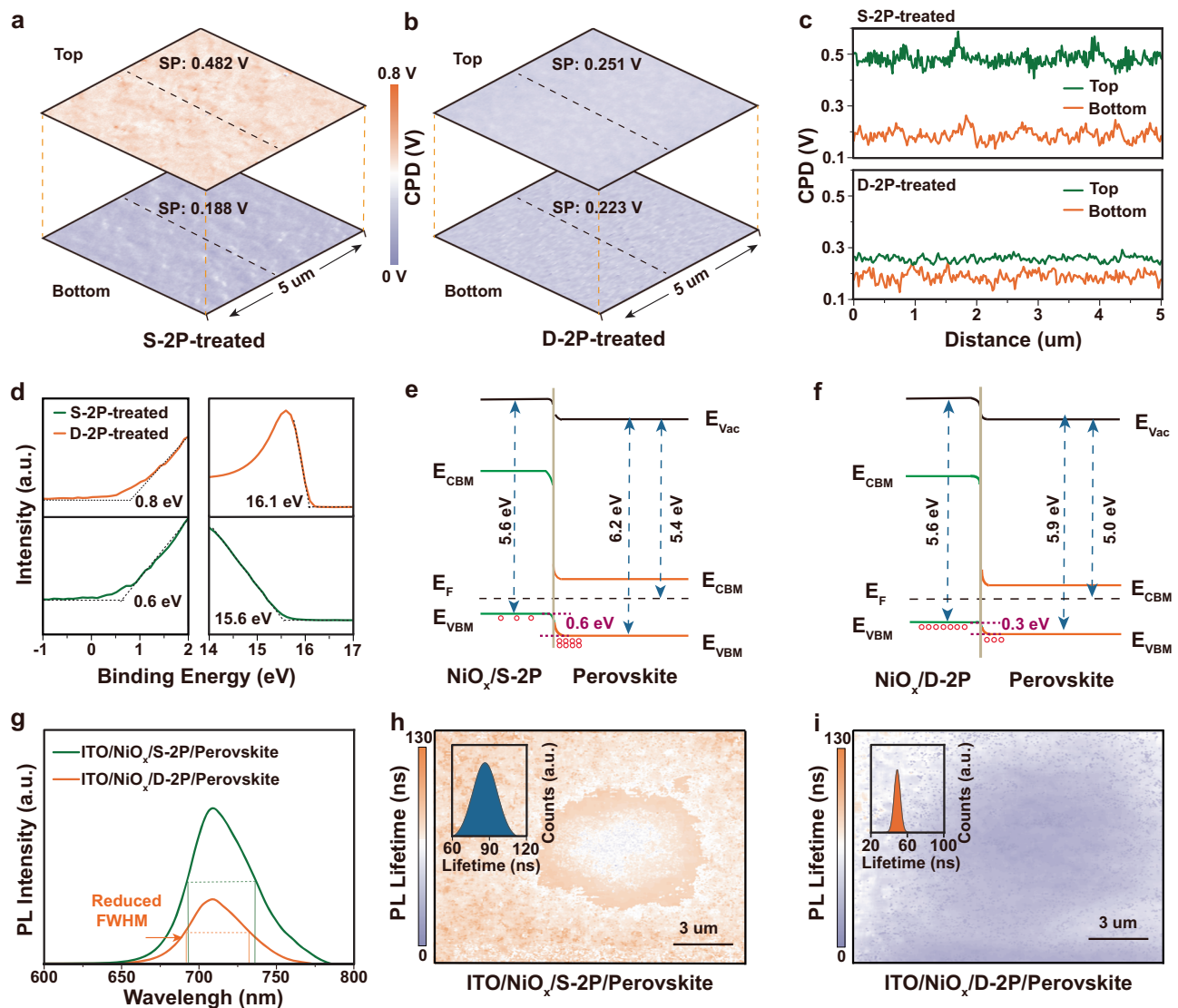
Fig. 3 | Carrier transport behavior of homogeneous halogen-phase perovskite film. a, b The spatial CPD maps and **c** extracted CPD line-scan spectra of S-2P-treated and D-2P-treated films. **d** UPS spectra of S-2P-treated and D-2P-treated perovskite films. Schematic representation of the energy bands for (**e**) S-2P-treated and **f** D-2P-treated perovskite films. **g** Steady-state PL spectra of ITO/NiO$_x$/S-2P/ Perovskite and ITO/NiO$_x$/D-2P/Perovskite films. Confocal PL lifetime mappings of (**h**) ITO/NiO$_x$/S-2P/Perovskite and (**i**) ITO/NiO$_x$/D-2P/Perovskite films. Inset: the extracted statistical PL lifetime distribution.

by current density-voltage (*J-V*) curve was verified by the external quantum efficiency (EQE) spectra (Supplementary Fig. 27). Moreover, the D-2P-treated PSC with high repeatability exhibited negligible hysteresis and stable maximum power point output (Supplementary Fig. 28, 29, Supplementary Table 3). We also investigated the effects of the number of 2P layer and the bilayer structure of other carbazole-phosphate-based acids on WBG PSCs (Supplementary Figs. 30–34, Supplementary Tables 4 and 5). In contrast, NiO$_x$-based D-SP-treated PSCs exhibited the best photovoltaic performance (Supplementary Figs. 35, 36, Supplementary Table 6). The remarkably high V_{oc} (1.32 V) can also be obtained, and reduced V_{oc} loss is a crucial factor in achieving PCE improvement.

The dependence of V_{oc} on illumination intensity is an effective strategy to evaluate the internal recombination mechanism in PSCs. The ideality factor *n* can be obtained by calculating the slope of the fitted straight line. As shown in Fig. 4d, D-2P-treated PSC displayed a smaller *n* value (1.21) than S-2P-treated PSC (1.88), and *n* value close to 1 indicates that Shockley-Read-Hall recombination is substantially suppressed. This can also be demonstrated by the low reverse saturation current under dark conditions (Supplementary Fig. 37). The larger

recombination resistance (R_{rec} = 22.52 KΩ) and smaller transport resistance (R_{tr} = 125.61 Ω) for D-2P-treated PSC corresponds to more efficient hole transport and extraction (Supplementary Fig. 38). Therefore, a longer charge-recombination lifetime (τ_{rec} = 53.33 μs) and a shorter charge-extraction time (τ_{tra} = 0.38 μs) were obtained according to the transient photovoltage (TPV) and transient photo-current (TPC) measurements (Supplementary Fig. 39). A similar conclusion could be also obtained from the capacitance-voltage (*C-V*) characteristics of PSCs (Fig. 4e). The D-2P-treated PSC displayed an increased built-in potential (V_{bi}) from 1.01 to 1.16 V, implying an enlarged driving force of carrier extraction and separation, which is contributing to the large V_{oc}[46]. To quantitatively evaluate and correlate the recombination rate with the V_{oc} and device performance, we operated solar cells as light-emitting diodes (Fig. 4f), as follows[47]:

$$V_{oc} = V_{oc,rad} - \frac{kT}{e} ln EQE_{EL}^{-1} \quad (1)$$

where $V_{oc,rad}$, EQE_{EL}, *k*, *T* and *e* are the radiative limit of V_{oc}, electroluminescence external quantum efficiency, Boltzmann's constant,
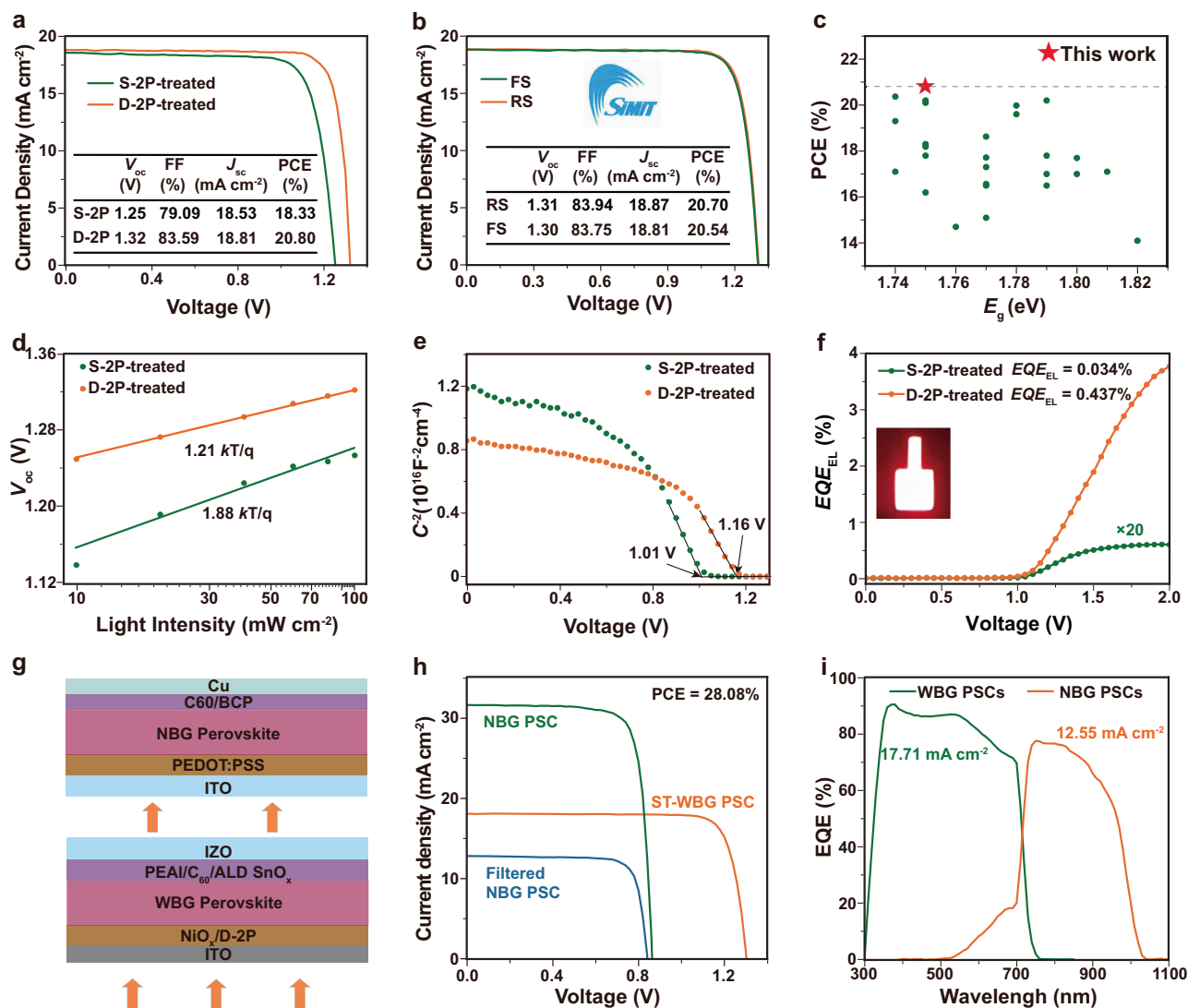
Fig. 4 | Photovoltaic performance and the V_{oc} loss mechanism. a J-V curves of S-2P-treated and D-2P-treated PSCs. **b** The certified J-V curves of the D-2P-treated PSC at SIMIT. **c** PCE comparison of our work and the reported PCE of WBG PSCs. **d** V_{oc} evolution of the devices under different illumination intensities. **e** C-V curves of S-2P-treated and D-2P-treated PSCs. **f** EQE_{EL} spectra of S-2P-treated and D-2P-treated devices. Inset: EL image of D-2P-treated devices. **g** Schematic diagram of device structure, **h** J-V curves, and **i** EQE spectra of 4-T all-perovskite tandem solar cell.

thermodynamic temperature and elementary charge. D-2P-treated device showed a detected EL emission even under a low bias voltage of 1.10 V (Supplementary Fig. 40). The V_{oc} loss was calculated by measuring the EQE_{EL} of the device. D-2P-treated device obtained an improved EQE_{EL} value (0.437%), which was an order of magnitude higher than S-2P-treated device (0.034%). This demonstrated the substantially reduced V_{oc} loss of 0.15 V, agreeing well with the improved V_{oc} of 1.32 V.

To show the application potential of WBG PSCs with D-2P structure, we fabricated a semitransparent device to construct four-terminal (4-T) all-perovskite tandem solar cell with NBG perovskite bottom cell[41,48] (Fig. 4g). The resulting semitransparent WBG PSC yielded a PCE of 19.35% with a V_{oc} of 1.30 V. The filtered NBG PSC possessed a PCE of 8.73% based on an initial PCE of 21.70% (Fig. 4h and Supplementary Table 7). The reduced PCE of the filtered NBG PSC is mainly ascribed to the sharp decline in J_{sc} from 31.52 to 12.87 mA cm^{-2}, which is in accordance with the corresponding EQE spectra (Fig. 4i). The most of the short wavelength photons (300 – 700 nm) can be absorbed by the top semitransparent PSC, which allows that the long wavelength photons are absorbed by the bottom PSC. As a result, 4-T

all-perovskite tandem solar cell achieved a PCE of 28.08%, which is one of the highest PCE reported for 4-T all-perovskite tandem cell.

Subsequently, we investigative the stability of WBG perovskite materials and photovoltaic devices. Residual lattice strain is usually one of the crucial factors affecting the stability of perovskite crystal structures, which could be characterized by grazing incident X-ray diffraction (GIXRD) via the 2θ-$\sin^2\varphi$ method[49,50]. As shown in Fig. 5a–c, D-2P-treated perovskite film displayed relieved lattice strain (10.0 MPa) compared to the S-2P-treated perovskite film (59.8 MPa), which is attributed to the homogeneous halogen-phase distribution. We evaluated the migration ability of halide ions by temperature-dependent conductivity measurements[51]. The ion migration activation energy (E_a) is obtained by fitting the corresponding plots with the Nernst-Einstein equation[52] (Fig. 5d). A larger E_a (0.58 eV) is observed in the D-2P-treated perovskite film than that in the S-2P-treated one (0.17 eV). The relieved lattice strain and increased halogen ion migration barrier facilitate the realization of robust stability of mixed-halide perovskite films. The EL spectra of PSCs at various bias voltages are showed in the Fig. 5e, f. Distinguishable phase separation can be observed in S-2P-treated PSC when the bias voltage exceeds 3.0 V. In
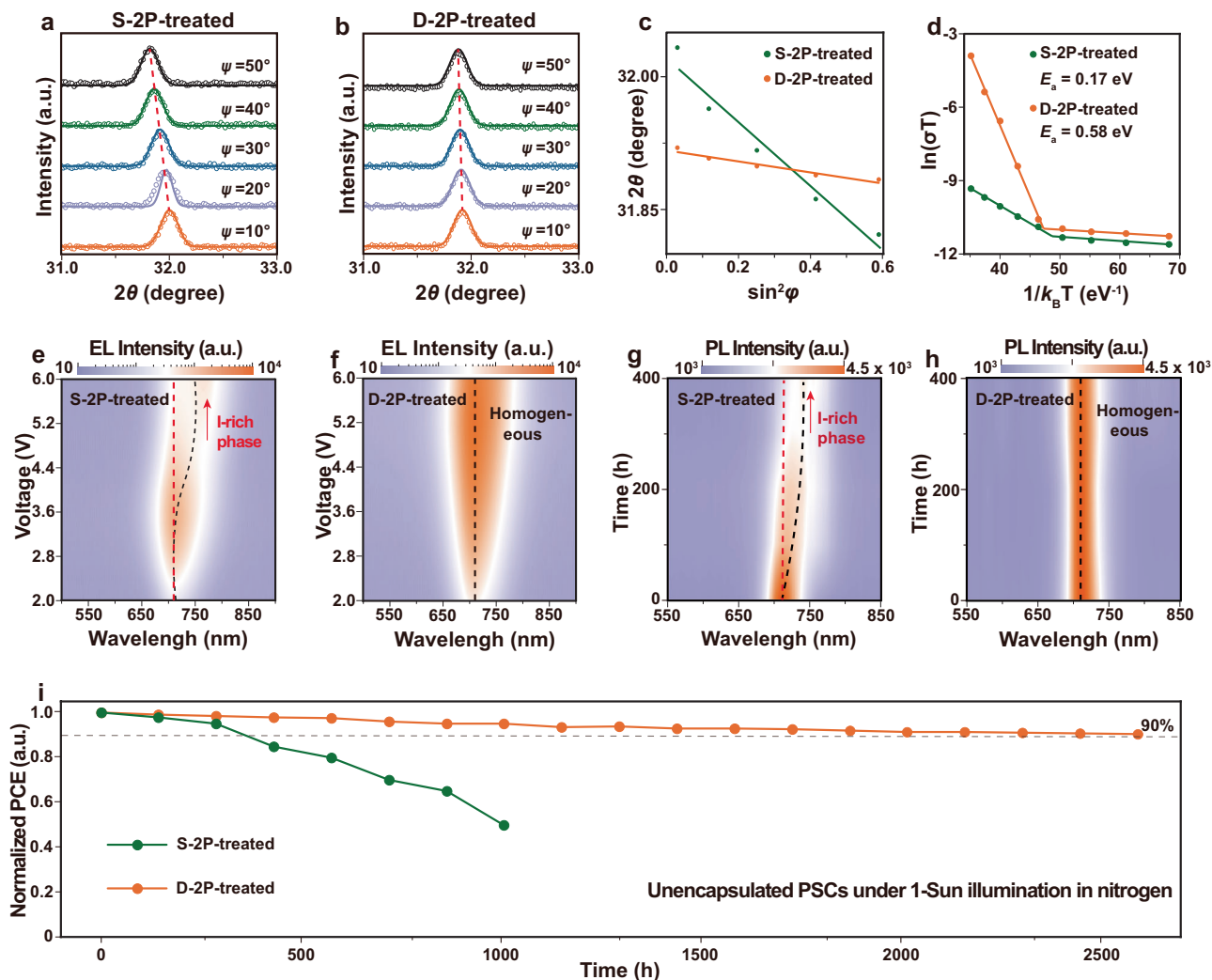
Fig. 5 | Residual strain of perovskite films and stability of solar cells. GIXRD patterns at different tilt angles for (**a**) S-2P-treated and (**b**) D-2P-treated perovskite films. **c** Linear fit of 2θ-$\sin^2\varphi$. **d** Temperature-dependent conductivity measurements of S-2P-treated and D-2P-treated perovskite films. EL spectra at various bias for (**e**) S-2P-treated and (**f**) D-2P-treated PSCs. Time-dependent PL spectra of (**g**) S-2P-treated and (**h**) D-2P-treated perovskite films. **i** PCE evolution curves for unencapsulated devices in N_2 environment.

contrast, D-2P-treated PSC exhibit continuously enhanced EL signals at constant wavelength with increasing bias voltage from 2.0 to 6.0 V. In addition to the improved electric field stability, the light stability of the D-2P-treated perovskite is also impressive.

Time-dependent PL measurements of perovskite films were carried out in air during continuous 1-sun light illumination (Fig. 5g, h). The D-2P-treated film still exhibited a constant PL intensity at 708 nm after 400 h, while the S-2P-treated perovskite film showed a split and blue-shifted PL peak after being soaked for a very short time. We further studied the phase separation of perovskite films under long-term light illumination conditions by the SEM coupled with EDS mappings (Supplementary Fig. 41). For perovskite films, the contents of I and Br elements are large enough, so the influence of possible presence of background noise on the analysis of their distribution is negligible. After two months of continuous light illumination, the S-2P-treated perovskite film showed an inhomogeneous halogen (Br and I) distribution compared with the pristine one. And no obvious holes were found in the main aggregation areas of I and Br elements. It can be observed that the halogen inhomogeneous perovskite phase at different film depths will aggravate the phase separation of the entire film. In contrast, the D-2P-treated perovskite film still exhibited homogeneous halogen distribution under the same light illumination

conditions. The electric field stability and light stability of perovskite film guarantee the long-term stability of solar cells. The PCE evolution of the unencapsulated WBG PSCs were monitored in accordance with the ISOS-L-1 test standard[53] (Fig. 5i). D-2P-treated PSC still maintained more than 90% of its initial PCE after continuous 1-sun illumination conditions in nitrogen for 2500 h, while the S-2P-treated device has rapidly degraded to less than half its initial PCE after only 1000 h.

Discussion

In conclusion, we demonstrate an efficient and stable WBG PSC with the homogeneous halogen-phase distribution. Guided by DFT calculations, we design the D-2P structure through π-π interactions between 2P molecules. The phosphate groups exposed on the surface of the D-2P structure provide nucleation sites for the homogeneous halogen-phase perovskite. Bottom-up templated crystallization results in the homogeneous perovskite phase distribution. The efficient carrier extraction between the perovskite and the charge transport layer reduces V_{oc} loss of WBG PSC. As a result, D-2P-treated PSC (1.75 eV) achieved a champion PCE of 20.80% (certified 20.70%), which is the highest value reported for a WBG PSC with a bandgap wider than 1.74 eV. Benefiting from improved electric field stability and light stability of perovskite film, the resulting PSC achieves improved long-

term stability, and maintained more than 90% of its initial PCE after continuous 1-sun illumination conditions for 2500 h. This work will provide a route for minimizing V_{oc} loss in WBG PSC, and pave the way for the development of perovskite tandem solar cells.

Methods
Materials
N,N-dimethylformamide (DMF, 99.8%, anhydrous), dimethylsulfoxide (DMSO, ≥ 99.9%, anhydrous), 2-Propanol (IPA, 99.5%, anhydrous) and chlorobenzene (CB, 99.8%, anhydrous) were obtained from Sigma-Aldrich. Tin (II) iodide (SnI_2, 99.99%) and tin (II) fluoride (SnF_2, 99%) were purchased from Sigma-Aldrich. Formamidinium iodide (FAI, 99.9%), methylammonium iodide (MAI, 99.9%), cesium iodide (CsI, 99.999%), lead iodide (PbI_2, 99.999%), lead bromide ($PbBr_2$, 99.999%), methylammonium chloride (MACl, 99.9%), 2-phenylethylamine hydroiodide (PEAI, 99.5%) and indium tin oxide (ITO, 15 Ω) glass were obtained from Advanced Election Technology Co., Ltd. [2-(9H-Carbazol-9-yl)ethyl]phosphonic Acid (2P, > 98%), [2-(3,6-Dimethoxy-9H-carbazol-9-yl)ethyl]phosphonic Acid (MeO-2PACz > 98%) and [4-(3,6-Dimethoxy-9H-carbazol-9-yl)butyl]phosphonic Acid (MeO-4PACz > 98%) were purchased from TCI. Nickel oxide (NiO_x, 99.999%) was from Xi 'an E-light New Material Co., LTD. Fullerene (C_{60}, 99.9%) and bathocuproine (BCP, 99%) were obtained from Xi'an Polymer Light Technology Corporation. PEDOT:PSS (CLEVIOS P VP AI 4083) was purchased from Heraeus, LLC. None of the above chemicals received further purification, were used directly.

Single-junction perovskite device fabrication
The pre-patterned ITO substrates were placed in cleaning agent, deionized water, anhydrous ethanol, and acetone in sequence cleaning for 20 min. The cleaned ITO substrates were treated with UV-zone for 20 min. NiO_x nanoparticles (10 mg) were dissolved in 1 ml of pure water, ultrasonic shock for 20 min, and then filtered by a filter head with an aperture of 0.22 μm for reserve use. The NiO_x film was prepared by spin-coating NiO_x solution on the ITO substrate at 3000 rpm for 30 s, and then annealed at 110 °C for 15 min in air. S-2P film is formed by spinning ethanol solution of 2P molecule coating at 3000 rpm for 30 s, annealing at 100 °C for 10 min, rinsing with anhydrous ethanol, repeat twice to form D-2P film. For 1.5 M $FA_{0.8}Cs_{0.15}MA_{0.05}Pb(I_{0.7}Br_{0.3})_3$ perovskite, PbI_2, $PbBr_2$, FAI, MAI and CsI are dissolved into a mixed solvent of DMF and DMSO (4:1) at the stoichiometric ratio. The perovskite layer was fabricated by spin coating 30 μl perovskite precursor solution at a speed of 5000 rpm for 32 s in a N_2 glovebox. At the time of 22 s, 110 μl CB was dropped as an anti-solvent. The fabricated film was annealed at 100 °C for 60 min. For PEAI treatment, the 3 mg PEAI was dissolved in 1 ml IPA and spin-coated onto the perovskite surface at 4000 rpm for 30 s. Finally, it is transferred to a high vacuum chamber (6×10^{-4} Pa), and the C_{60} (35 nm), BCP (6 nm) and Ag (100 nm) are thermally evaporated.

4 T all-perovskite tandem cells Fabrication
Semi-transparent WBG PSCs. Preparation of WBG perovskite films as shown above, after depositing 35 nm C_{60}, the substrates were then transferred to the atomic layer deposition (ALD) system where 40 nm of SnO_2 was deposited at 80 °C. Next, a 100 nm-thick indium zinc oxide film (IZO) was sputtered.

NBG PSCs. The PEDOT:PSS solution was spin-coated onto ITO and annealed in air at 100 °C for 15 min. Immediately after annealing the substrates were placed in the glove box to deposit NBG perovskite films. For 2 M $FAPb_{0.5}Sn_{0.5}I_3$ perovskite, PbI_2, FAI, SnI_2, and SnF_2 are dissolved into a mixed solvent of DMF and DMSO (2:1) at the stoichiometric ratio. NBG perovskite precursor solution was deposited on the substrate by two-part spin coating process: 1000 rpm for 10 s and

4000 rpm for 50 s. At the last 20 s, 200 μl of CB was dripped and then annealed at 100 °C for 10 min. Finally, it was transferred to the evaporation system, depositing 35 nm C_{60}, 6 nm BCP and 100 nm Ag, respectively.

Device characterization
The V_{oc} and J_{sc} were measured using a Keithley 2400 instrument. Instantaneous J-V curves then measured with a scanning rate of 100 mV s^{-1} (voltage step of 20 mV and delay time of 200 ms). The devices were measured by a customized mask with an effective area of 0.089 cm^{-2}. The output of the light source was adjusted using a calibrated silicon photodiode (Newport) at 1 sun (100 mW cm^{-2}). The J-V curves is measured in atmospheric conditions. Through the silicon standard cells (SRC-00288, Enli Tech) and sun simulator (SS-F5, Enli Tech) for light intensity calibration. Electroluminescence efficiency (EQE_{EL}) was performed via a system containing a Keithley 2400 digital source meter for current injection, a Keithley 6482 picometer, and the Si photodiode for quantifying the photons emitted from PSCs.

Other characterizations
The in-situ GIWAXS measurements were performed at BL 17B1 beamline of the Shanghai Synchrotron Radiation Facility (SSRF). X-ray with a wavelength of 1.238 Å was utilized for incident-angle-depending measurements, and the incident angle was fixed at 0.3° and 1°. GIWAXS data was collected at every 1 s. The ex-situ GIWAXS patterns with various grazing incident angles of perovskite films were measured using monochromatic beam (1.54 Å) on the beamline 1W1A at Beijing Synchrotron Radiation Facility (BSRF), China. The XPS was measured at a vacuum chamber (ESCALAB 250Xi), with a base pressure of 2×10^{-10} mbar, for XPS depth profiling measurements. XPS measurements were performed using a double-differentially pumped He gas discharge lamp emitting He I radiation ($hv = 21.22$ eV).

Reporting summary
Further information on research design is available in the Nature Portfolio Reporting Summary linked to this article.

Data availability
All the data supporting the findings of this study are available within this article and its Supplementary Information. Any additional information can be obtained from corresponding authors upon request. Source data are provided with this paper.

References
1. Brinkmann, K. O. et al. Perovskite-organic tandem solar cells with indium oxide interconnect. *Nature* **604**, 280–286 (2022).
2. Chen, W. et al. Monolithic perovskite/organic tandem solar cells with 23.6% efficiency enabled by reduced voltage losses and optimized interconnecting layer. *Nat. Energy* **7**, 229–237 (2022).
3. He, R. et al. Wide-bandgap organic-inorganic hybrid and all-inorganic perovskite solar cells and their application in all-perovskite tandem solar cells. *Energy Environ. Sci.* **14**, 5723–5759 (2021).
4. De et al. Bifacial perovskite/silicon tandem solar cells. *Joule* **6**, 1431–1445 (2022).
5. Roger, J. et al. Laminated monolithic perovskite/silicon tandem photovoltaics. *Adv. Energy Mater.* **12**, 2200961 (2022).
6. Wen, J. et al. Steric engineering enables efficient and photostable wide-bandgap perovskites for all-perovskite tandem solar cells. *Adv. Mater.* **34**, 2110356 (2022).
7. Jiang, Q. et al. Compositional texture engineering for highly stable wide-bandgap perovskite solar cells. *Science* **378**, 1295–1300 (2022).
8. Mahesh, S. et al. Revealing the origin of voltage loss in mixed-halide perovskite solar cells. *Energy Environ. Sci.* **13**, 258–267 (2020).

9. Zhao, Y. et al. Reduced 0.418 V V_{oc}-deficit of 1.73 eV wide-bandgap perovskite solar cells assisted by dual chlorides for efficient all-perovskite tandems. *Energy Environ. Sci.* **16**, 2080–2089 (2023).

10. Cui, H. et al. Lead halide coordination competition at buried interfaces for low V_{oc}-deficits in wide-bandgap perovskite solar cells. *Energy Environ. Sci.* **16**, 5992–6002 (2023).

11. Wang, Y., Mahmoudi, T. & Hahn, Y. B. Highly stable and efficient perovskite solar cells based on FAMA-perovskite-Cu: NiO composites with 20.7% efficiency and 80.5% fill factor. *Adv. Energy Mater.* **10**, 2000967 (2020).

12. Bai, S. et al. Planar perovskite solar cells with long-term stability using ionic liquid additives. *Nature* **571**, 245–250 (2019).

13. Li, R. et al. $CsPbCl_3$-cluster-widened bandgap and inhibited phase segregation in a wide-bandgap perovskite and its application to NiO_x-based perovskite/silicon tandem solar cells. *Adv. Mater.* **34**, 2201451 (2022).

14. Zhang, S. et al. Minimizing buried interfacial defects for efficient inverted perovskite solar cells. *Science* **380**, 404–409 (2023).

15. Li, T. et al. Inorganic wide-bandgap perovskite subcells with dipole bridge for all-perovskite tandems. *Nat. Energy* **8**, 610–620 (2023).

16. Li, H. et al. Intermolecular π-π conjugation self-assembly to stabilize surface passivation of highly efficient perovskite solar cells. *Adv. Mater.* **32**, 1907396 (2020).

17. Lai, H. et al. High-performance flexible all-perovskite tandem solar cells with reduced V_{oc}-deficit in wide-bandgap subcell. *Adv. Energy Mater.* **12**, 2202438 (2022).

18. Yang, W. et al. Unlocking voltage potentials of mixed-halide perovskite solar cells via phase segregation suppression. *Adv. Funct. Mater.* **32**, 2110698 (2021).

19. Zheng, Y. et al. Downward homogenized crystallization for inverted wide-bandgap mixed-halide perovskite solar cells with 21% efficiency and suppressed photo-induced halide segregation. *Adv. Funct. Mater.* **32**, 2200431 (2022).

20. Chen, S. et al. Crystallization in one-step solution deposition of perovskite films: upward or downward? *Sci. Adv.* **7**, eabb2412 (2021).

21. He, T., Jiang, Y., Xing, X. & Yuan, M. Structured perovskite light absorbers for efficient and stable photovoltaics. *Adv. Mater.* **32**, 1903937 (2020).

22. He, T. et al. Reduced-dimensional perovskite photovoltaics with homogeneous energy landscape. *Nat. Commun.* **11**, 1672 (2020).

23. Liang, C. et al. Two-dimensional ruddlesden-popper layered perovskite solar cells based on phase-pure thin films. *Nat. Energy* **6**, 38–45 (2021).

24. Liang, Z. et al. Homogenizing out-of-plane cation composition in perovskite solar cells. *Nature* **624**, 557–563 (2023).

25. Guo, R. et al. Tailoring multifunctional self-assembled hole transporting molecules for highly efficient and stable inverted perovskite solar cells. *Adv. Funct. Mater.* **33**, 2211955 (2023).

26. Kim, J. H., Schembri, T., Bialas, D., Stolte, M. & Wurthner, F. Slip-stacked j-aggregate materials for organic solar cells and photodetectors. *Adv. Mater.* **34**, 2104678 (2022).

27. Alghamdi, A. R. M., Yanagida, M., Shirai, Y., Andersson, G. G. & Miyano, K. Surface passivation of sputtered NiO_x using a SAM interface layer to enhance the performance of perovskite solar cells. *ACS Omega* **7**, 12147–12157 (2022).

28. Li, X. et al. Improved performance and stability of perovskite solar cells by crystal crosslinking with alkylphosphonic acid omega-ammonium chlorides. *Nat. Chem.* **7**, 703–711 (2015).

29. Qin, M., Chan, P. F. & Lu, X. A systematic review of metal halide perovskite crystallization and film formation mechanism unveiled by in situ GIWAXS. *Adv. Mater.* **33**, 2105290 (2021).

30. Liu, L. et al. Self-assembled amphiphilic monolayer for efficient and stable wide-bandgap perovskite solar cells. *Adv. Energy Mater.* **13**, 2202802 (2023).

31. Ou, Y. et al. Collaborative interfacial modification and surficial passivation for high-efficiency MA-free wide-bandgap perovskite solar cells. *Chem. Eng. J.* **469**, 143860 (2023).

32. Pratap, S. et al. Out-of-equilibrium processes in crystallization of organic-inorganic perovskites during spin coating. *Nat. Commun.* **12**, 5624 (2021).

33. Sung, S. J. et al. Molecular engineering for function-tailored interface modifier in high-performance perovskite solar cells. *Adv. Energy Mater.* **12**, 2200758 (2022).

34. Bi, H. et al. Perovskite solar cells consisting of PTAA modified with monomolecular layer and application to all-perovskite tandem solar cells with efficiency over 25. *Adv. Funct. Mater.* **33**, 2300089 (2023).

35. Han, H. et al. Anti-phase boundary accelerated exsolution of nanoparticles in non-stoichiometric perovskite thin films. *Nat. Commun.* **13**, 6682 (2022).

36. Wei, K. et al. Facile exfoliation of the perovskite thin film for visualizing the buried interfaces in perovskite solar cells. *ACS Appl. Energy Mater.* **5**, 7458–7465 (2022).

37. Kim, D. et al. Microstructural evaluation of phase instability in large bandgap metal halide perovskites. *ACS Nano* **15**, 20391–20402 (2021).

38. Lee, H. et al. In situ observation of photoinduced halide segregation in mixed halide perovskite. *ACS Appl. Energy Mater.* **6**, 1565–1574 (2023).

39. Chen, S. et al. Thermal and light induced surface instability of perovskite films in the photoelectron spectroscopy measurement. *J. Electron. Spectrosc. Relat. Phenom.* **229**, 108–113 (2018).

40. Li, Y. et al. Homologous bromides treatment for improving the open-circuit voltage of perovskite solar cells. *Adv. Mater.* **34**, 2106280 (2022).

41. Lin, R. et al. All-perovskite tandem solar cells with 3D/3D bilayer perovskite heterojunction. *Nature* **620**, 994–1000 (2023).

42. Kirchartz, T., Márquez, J. A., Stolterfoht, M. & Unold, T. Photoluminescence-based characterization of halide perovskites for photovoltaics. *Adv. Energy Mater.* **10**, 1904134 (2020).

43. Duan, H. S. et al. The identification and characterization of defect states in hybrid organic-inorganic perovskite photovoltaics. *Phys. Chem. Chem. Phys.* **17**, 112–116 (2015).

44. Wu, W. et al. Molecular doping enabled scalable blading of efficient hole-transport-layer-free perovskite solar cells. *Nat. Commun.* **9**, 1–8 (2018).

45. Liu, S. et al. Buried interface molecular hybrid for inverted perovskite solar cells. *Nature* **632**, 536–542 (2024).

46. Zhao, D. et al. Efficient two-terminal all-perovskite tandem solar cells enabled by high-quality low-bandgap absorber layers. *Nat. Energy* **3**, 1093–1100 (2018).

47. Ross, R. T. Some thermodynamics of photochemical systems. *J. Chem. Phys.* **46**, 4590–4593 (1967).

48. Li, L. et al. Flexible all-perovskite tandem solar cells approaching 25% efficiency with molecule-bridged hole-selective contact. *Nat. Energy* **7**, 708–717 (2022).

49. Zhu, C. et al. Strain engineering in perovskite solar cells and its impacts on carrier dynamics. *Nat. Commun.* **10**, 815 (2019).

50. Li, X. et al. Strain regulation of mixed-halide perovskites enables high-performance wide-bandgap photovoltaics. *Adv. Mater.* **36**, 2401103 (2024).

51. Zhao, J. et al. Strained hybrid perovskite thin films and their impact on the intrinsic stability of perovskite solar cells. *Sci. Adv.* **3**, eaao5616 (2017).

52. Yang, S. et al. Stabilizing halide perovskite surfaces for solar cell operation with wide-bandgap lead oxysalts. *Science* **365**, 473–478 (2019).

53. Reese, M. O. et al. Consensus stability testing protocols for organic photovoltaic materials and devices. *Sol. Energy Mater. Sol. Cells* **95**, 1253–1267 (2011).

Author contributions

R.W., X.L., and S.Y. contributed equally to this work. T.H. conceived the idea and supervised the work. R.W., X.L., and S.Y. fabricated devices and analyzed the data. R.W., N.M., S.M.H.Q., and X.Z. performed DFT simulation. Y.C. and H.L. guided the GIWAXS and GIXRD measurements. R.W. and X.L cowrote the paper. S.M.H.Q., R.W., X.L., M.Y., and T.H. revised the paper. All authors read and commented on the paper.

Competing interests

The authors declare no competing interests.

Additional information

Supplementary information The online version contains supplementary material available at https://doi.org/10.1038/s41467-024-53344-9.

Correspondence and requests for materials should be addressed to Shaopeng Yang or Tingwei He.

Peer review information *Nature Communications* thanks the anonymous, reviewers for their contribution to the peer review of this work. A peer review file is available.

Reprints and permissions information is available at http://www.nature.com/reprints

Publisher's note Springer Nature remains neutral with regard to jurisdictional claims in published maps and institutional affiliations.